

Scale Space Analysis and Active Contours for Omnidirectional Images

Iva Bogdanova, Xavier Bresson, Jean-Philippe Thiran, *Senior Member, IEEE*, and Pierre Vanderghenst, *Member, IEEE*

Abstract—A new generation of optical devices that generate images covering a larger part of the field of view than conventional cameras, namely catadioptric cameras, is slowly emerging. These omnidirectional images will most probably deeply impact computer vision in the forthcoming years, provided that the necessary algorithmic background stands strong. In this paper, we propose a general framework that helps define various computer vision primitives. We show that geometry, which plays a central role in the formation of omnidirectional images, must be carefully taken into account while performing such simple tasks as smoothing or edge detection. Partial differential equations (PDEs) offer a very versatile tool that is well suited to cope with geometrical constraints. We derive new energy functionals and PDEs for segmenting images obtained from catadioptric cameras and show that they can be implemented robustly using classical finite difference schemes. Various experimental results illustrate the potential of these new methods on both synthetic and natural images.

I. INTRODUCTION

CONVENTIONAL imaging systems are severely limited in their field of view so that, in order to obtain an image of an entire scene, either multiple or rotating cameras must be used. However, in many cases, a rotating camera is not suitable because it cannot simultaneously cover all directions of a dynamic scene. On the other hand, mechanical parts are usually heavy and expensive to manufacture. An interesting alternative way to enhance the field of view is to use mirrors in conjunction with lenses. A catadioptric sensor is an imaging sensor based on the combination of a curved mirror and a lens to form a projection onto the image plane of a camera (see Fig. 1). Such a sensor is capable of recording light rays coming from a broad range of directions around the focal point of the mirror. Consequently,

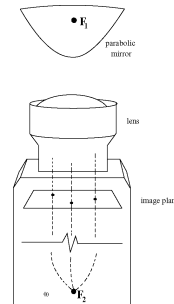


Fig. 1. Catadioptric imaging system.

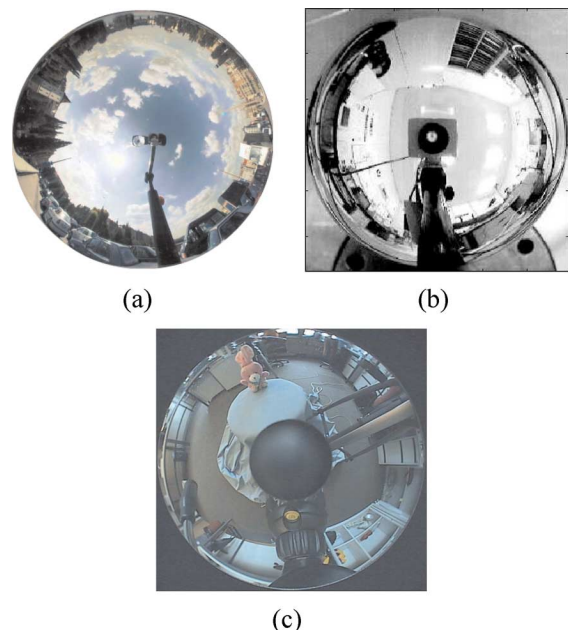


Fig. 2. Examples of omnidirectional images obtained using different mirrors: (a) hyperbolic, (b) spherical, and (c) parabolic.

the images obtained from these sensors are often called omnidirectional because they contain the information from a scene in all possible directions around a perfect point-wise observer.

Various mirror shapes can be used but it has been shown in [1] that the cases of interest are spherical, hyperbolic and parabolic mirrors, among which only the last two have a single effective viewpoint. Examples of images acquired using catadioptric cameras are provided in Fig. 2.

Obviously, the sensor records a distorted image. The formation of the omnidirectional image is well controlled and allows us to easily derive its geometrical properties. First, the mirror is a surface \mathcal{M} in \mathbb{R}^3 whose geometrical properties are encoded

Manuscript received September 1, 2006; revised February 21, 2007. I. Bogdanova and P. Vanderghenst were supported by the Swiss National Science Foundation under Grant FNS 200021-101880/1. X. Bresson was supported in part by the National Science Foundation under Grant DMS-0610079 and in part by the Office of Naval Research under Grant N00014-06-1-0345. The associate editor coordinating the review of this manuscript and approving it for publication was Prof. Vicent Caselles.

I. Bogdanova is with the Institute of Microtechnology, Université de Neuchâtel, 2000 Neuchâtel, Switzerland, and also with the Signal Processing Institute, Station 11, Ecole Polytechnique Fédérale de Lausanne (EPFL), 1015 Lausanne, Switzerland (e-mail: iva.bogdanova@unine.ch).

X. Bresson is with the Signal Processing Institute, Station 11, Ecole Polytechnique Fédérale de Lausanne (EPFL), 1015 Lausanne, Switzerland, and also with the Department of Mathematics, University of California, Los Angeles, CA 90095-1555 USA (e-mail: xbresson@math.ucla.edu).

J.-P. Thiran and P. Vanderghenst are with the Signal Processing Institute, Station 11, Ecole Polytechnique Fédérale de Lausanne (EPFL), 1015 Lausanne, Switzerland (e-mail: jean-philippe.thiran@epfl.ch; pierre.vanderghenst@epfl.ch).

Color versions of one or more of the figures in this paper are available online at <http://ieeexplore.ieee.org>.

Digital Object Identifier 10.1109/TIP.2007.899008

in its induced Riemannian metric g_{ij} . Second, and since we are considering perfect quadrics only, any light ray incident on one of the foci of the mirror is reflected to the other focus. A pixel is then created where the reflected light ray intersects the camera plane. Let (x, y) and (x_0, x_1, x_2) label coordinates in the image plane, here an open subset $\Omega \subseteq \mathbb{R}^2$, and on the mirror surface, respectively. The whole image formation process depicted above induces a mapping between manifolds from the surface of the mirror to the camera plane

$$\begin{aligned}\Phi : \mathcal{M} &\mapsto \Omega \\ (x_0, x_1, x_2) &\mapsto (x, y).\end{aligned}$$

This application allows us to transport the metric $g_{ij}(x_0, x_1, x_2)$ and equip the image with a pullback metric $h_{ij}(x, y)$

$$h_{jl} = \frac{\partial}{\partial u_j} x_r \frac{\partial}{\partial u_l} x_s g_{rs}, \quad j, l \in \{1, 2\}, r, s \in \{0, 1, 2\} \quad (1)$$

where we set $u_1 = x$, $u_2 = y$ and Einstein's summation convention has been used. Two comments are in order here. First, it should be noted that the image plane (Ω, h) should not be dealt with as the familiar Euclidean plane. It carries a very specific geometry encoded in its metric h_{ij} . Second, this geometry is really inherited from that of the mirror (\mathcal{M}, g) , but realized using a more conventional domain $\Omega \subseteq \mathbb{R}^2$. This simple, yet geometrically accurate, parameterization will be most helpful to perform computation on \mathcal{M} . Besides (\mathcal{M}, g) and (Ω, h) , there is another manifold of interest for omnidirectional images: the 2-D sphere S^2 in \mathbb{R}^3 . It is, indeed, very interesting to be able to reconstruct the whole visual information around a perfect point-like observer standing at the focus of the mirror. In this case, each point $(\theta, \varphi) \in S^2$ represents the direction of an incoming light ray. For simple mirrors, it is possible to reconstruct this information directly from the omnidirectional image in the sensor plane Ω .

As we shall see throughout this paper, the geometry embodied by the metrics g or h is of primal importance. We will, thus, treat omnidirectional images as scalar fields on parametric manifolds. Geometry and, more particularly, the Riemannian structure will be used to derive generalizations of the concepts of smoothing, scale-space and geodesic active contours for this particular kind of images. We will proceed by deriving a fairly general framework based on energy minimization and partial differential equations (PDEs). Moreover, we will make use of the parameterization to compute efficiently these operations directly from the camera plane. These techniques are of course directly applicable to situations where scalar data are drawn on a parametric surface \mathcal{M} for which we have a decent projection to a euclidean parametric base Ω . In these cases, the framework derived in this paper allows to efficiently implement the above-mentioned algorithms directly in the parametric cartesian coordinates, with well-studied numerical schemes, while still respecting the complex geometry of the manifold.

This paper is organized as follows. In Section II, we review the geometry of the problem, particularizing to catadioptric systems. In Section III, we introduce basic differential operators on

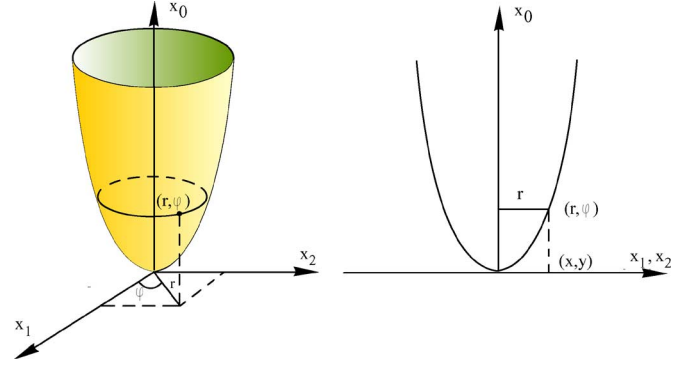


Fig. 3. Geometry of the paraboloid \mathcal{P}^2 embedded in \mathbb{R}^3 . Left: Original coordinates (x_0, x_1, x_2) expressed in polar coordinates (r, φ) are mapped to coordinates (x, y) after focal projection. Right: Focal projection coincides with a simple orthographic projection in this case.

Riemannian manifolds and provide explicit formulas for the surfaces of interest in this paper. Section IV is the core of the paper, where we construct active contours on parametric surfaces. The case of surfaces conformally euclidean is solved by a straightforward extension of the technique originally introduced in [2]. For more complex situations, we formulate a new energy minimization problem inspired by the formalism introduced in [3]. We illustrate our results with numerical simulations using omnidirectional images but also on generic situations where data is defined on surfaces. Finally, Section V gathers conclusions and suggestions for future research.

II. RIEMANNIAN GEOMETRY OF PARAMETRIC SURFACES

In this section, we introduce a few concepts of Riemannian geometry that will be used throughout this paper. This material is classical and can be found in standard textbooks (see for example [4]), but we include it here for clarity and as a way to introduce notations. These notions are first worked out in the case of omnidirectional images produced with parabolic catadioptric mirrors, which will be our main application. Since the techniques designed in this paper are fairly general, we also give explicit derivations in the case of scalar images drawn on the surface of a hyperboloid. These two case studies will be used later on in the paper in a recurrent way.

A. Parabolic Catadioptric Mirrors

A complete geometrical view of catadioptric systems has been worked out in [1], to which we refer for details. That paper shows that the most interesting catadioptric systems use either a parabolic or hyperbolic mirror. We will deal here with parabolic mirrors only, as they are by far the most common. None of our results are strictly bound to this particular case, though. In fact the techniques introduced below could be used for any mirror represented as a parametric surface.

The paraboloid \mathcal{P}^2 is a quadratic surface which can be expressed by the Cartesian equation

$$x_0 = b(x_1^2 + x_2^2). \quad (2)$$

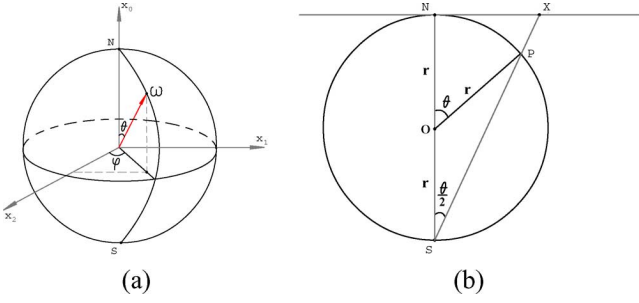


Fig. 4. Geometry of the 2-sphere: (a) spherical polar coordinates and (b) stereographic projection.

We will set $b = 1$ for simplicity. Using a system of polar coordinates (r, φ) shown in Fig. 3, we obtain the equivalent parameterization

$$x_0 = r^2 \quad (3)$$

$$x_1 = r \cos \varphi, \quad 0 \leq \varphi < 2\pi, \quad r \geq 0 \quad (4)$$

$$x_2 = r \sin \varphi. \quad (5)$$

The Euclidean line element can be expressed in these coordinates

$$dl^2 = dx_0^2 + dx_1^2 + dx_2^2 = (1 + 4r^2)dr^2 + r^2 d\varphi^2 \quad (6)$$

and this immediately gives us the metric on \mathcal{P}^2

$$g_{ij}(r, \varphi) = \begin{pmatrix} 1 + 4r^2 & 0 \\ 0 & r^2 \end{pmatrix}.$$

As shown by Geyer and Daniilidis in [1], any light ray incident to the focus of the paraboloid is going to be reflected to the other focus, here the point at infinity. Thus, the focal projection Φ from the mirror \mathcal{M} to the camera plane is simply the orthographic projection, i.e., the coordinates of the intersection between the reflected light ray and the camera plane are simply $(x, y) = (x_1, x_2)$. In the following, we shall need the induced metric on the camera plane in (x, y) coordinates. Since we have $r^2 = x^2 + y^2$ and $\varphi = \arctan(y/x)$, performing this change of variable in the 2-D Euclidean line element yields

$$dl^2 = (1 + 4x^2)dx^2 + 8xydxdy + (1 + 4y^2)dy^2 \quad (7)$$

which corresponds to the following metric:

$$h_{ij}(x, y) = \begin{pmatrix} 1 + 4x^2 & 4xy \\ 4xy & 1 + 4y^2 \end{pmatrix}. \quad (8)$$

Note that this metric is not diagonal; it will be an important source of complication later on.

In the case of a parabolic mirror, Geyer and Daniilidis showed that the reconstruction of a perfect viewpoint at the focus of the mirror can be simply computed as the inverse stereographic projection of the sensor image. It is, thus, also important to work out the links between the geometry of S^2 and that of the sensor image. As we shall see in the next sections, this will allow us to process the spherical image directly using the sensor output. Consider a sphere of radius r as depicted in Fig. 4. A point on S^2 is identified with the vector $(x_0, x_1, x_2) \equiv (r \cos \theta, r \sin \theta \sin \varphi, r \sin \theta \cos \varphi)$, $\theta \in [0, \pi)$,

$\varphi \in [0, 2\pi)$. In cartesian and polar (ρ, θ, φ) coordinates, the Euclidean line element reads

$$dl^2 = dx_0^2 + dx_1^2 + dx_2^2 = d\rho^2 + \rho^2(d\theta^2 + \sin^2 \theta d\varphi^2). \quad (9)$$

On the surface, $\rho = r$ and the differential $d\rho = 0$, so the metric induced on the sphere is given by the well-known expression

$$dl^2 = r^2(d\theta^2 + \sin^2 \theta d\varphi^2). \quad (10)$$

The stereographic projection sends a point (θ, φ) on the sphere to the point with polar coordinates (R, φ) in the plane, for which we have $\varphi = \varphi$, $R = r(1/2) \tan \theta/2$. It is shown in Fig. 4. In terms of these new coordinates, the metric becomes

$$dl^2 = \frac{4r^4}{(r^2 + R^2)^2} (dR^2 + R^2 d\varphi^2). \quad (11)$$

Let us proceed toward deriving the metric in cartesian sensor coordinates $(x, y) \in \mathbb{R}^2$, where $R^2 = x^2 + y^2$. We obtain

$$dl^2 = \frac{4r^4}{(r^2 + x^2 + y^2)^2} (dx^2 + dy^2). \quad (12)$$

In this case, the metric on the sphere is obtained from the metric on the Euclidean plane by multiplying the latter by the function $4r^2/(r^2 + x^2 + y^2)^2$

$$dl_{S^2}^2 = \frac{4r^4}{(r^2 + x^2 + y^2)^2} dl_{\mathbb{R}^2}^2. \quad (13)$$

Accordingly, the metric induced on \mathbb{R}^2 when $R = 1$ is derived as

$$h_{ij}(x, y) = \begin{pmatrix} \frac{4}{(1+x^2+y^2)^2} & 0 \\ 0 & \frac{4}{(1+x^2+y^2)^2} \end{pmatrix} \quad (14)$$

and, consequently, the inverse metric is as follows:

$$h^{ij}(x, y) = \begin{pmatrix} \frac{(1+x^2+y^2)^2}{4} & 0 \\ 0 & \frac{(1+x^2+y^2)^2}{4} \end{pmatrix}. \quad (15)$$

Metrics that differ only by a multiplicative factor are conformally equivalent. The stereographic projection endows the plane with a metric conformal to the regular euclidean metric. This particular class of problems will receive special attention later on in this paper. Finally, one should not be surprised that metrics (8) and (14) are so different. Though the related images are produced by the same system, the first one corresponds to light intensity on the parabolic mirror while the second one corresponds to light intensity perceived by an observer at the focus of the mirror. The same sensor image is, thus, endowed with different geometries, depending on which information one wishes to process.

B. Another Illustrative Example

Let us now give another illustrative example: a different parametric surface, together with a projection to a parametric base. Consider the two-sheeted hyperboloid H^2 depicted in Fig. 5. It is convenient to embed H^2 into the pseudo-Euclidean (or Minkowski) space \mathbb{R}_1^2 , whose line element is

$$dl^2 = dx_0^2 - dx_1^2 - dx_2^2. \quad (16)$$

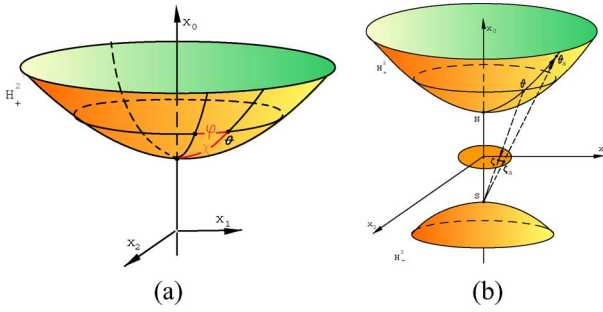


Fig. 5. Geometry of the 2-hyperboloid: (a) hyperbolic polar coordinates and (b) stereographic projection.

In these coordinates, H^2 is conveniently realized a pseudosphere of equation

$$x_0^2 - x_1^2 - x_2^2 = R^2.$$

In pseudo-polar coordinates $(x_0, x_1, x_2) \equiv (\rho \cosh \chi, \rho \sinh \chi \cos \varphi, \rho \sinh \chi \sin \varphi)$, (16) becomes

$$dl^2 = -\rho^2(d\chi^2 + \sinh^2 \chi d\varphi^2) + d\rho^2. \quad (17)$$

For $\rho = R$, we distinguish the upper sheet of the hyperboloid, and for $\rho = -R$, the lower one. Since ρ is constant on the hyperboloid, we finally have

$$-dl^2 = R^2(d\chi^2 + \sinh^2 \chi d\varphi^2) \quad (18)$$

and the metric on the upper sheet of H^2 reads

$$g_{ij}(\chi, \varphi) = \begin{pmatrix} 1 & 0 \\ 0 & \sinh^2 \chi \end{pmatrix}$$

where we set $R = 1$.

A useful parametric realization of the upper sheet of the hyperboloid consists in projecting inside the open unit disk in \mathbb{R}^2 by means of a stereographic projection (see Fig. 5)

$$x = \tanh \frac{\chi}{2} \cos \varphi \quad (19)$$

$$y = \tanh \frac{\chi}{2} \sin \varphi. \quad (20)$$

Note that, if the eccentricity of the hyperboloid is big enough, this mapping closely matches the focal projection of a hyperbolic mirror and can be used for omnidirectional image processing as well. The induced metric in the disk is easily computed

$$h_{ij}(x, y) = \begin{pmatrix} \frac{4}{(1-(x^2+y^2))^2} & 0 \\ 0 & \frac{4}{(1-(x^2+y^2))^2} \end{pmatrix}. \quad (21)$$

Note the formal similarities with the expressions derived above for the sphere and the general form of this metric, which is also conformally equivalent to the euclidean one.

Before concluding this section, we may wonder why one would work on the manifold-bound data instead of simply considering the acquired image as a regular euclidean one. We do believe there are simple tasks that can be performed directly on the sensor image, without resorting to the complex

framework discussed hereafter. However, there are important situations where working on the manifold is of vital importance. For example, it has been shown in [5] that working with a full field of view (a perfect omnidirectional image) stabilizes the structure from motion problem and that the reason for this gain is purely geometrical. Working with the image as observed by an observer at the focus of the mirror has also numerous advantages for tracking, since it processes the field of view in its natural coordinates. Finally, using the correct geometry is also of paramount importance in pattern recognition: on the sensor output seen as a regular euclidean image, objects of the same size or shape will appear distorted depending on their position, whereas these effects are nicely compensated for in the correct geometry. We will give a concrete example of these effects in Section IV-C.

III. SMOOTHING AND DETECTING EDGES ON PARAMETRIC MANIFOLDS

A. Warm-Up: Useful Differential Operators

Various classical tasks in Computer Vision (smoothing, edge detection) can be implemented by means of differential operators acting on images. Since we have defined omnidirectional images as scalar functions on Riemannian manifolds, we can now easily define the corresponding differential operators in the correct geometry. Even though most of this material can be found in standard textbooks [4], we provide here the most important expressions for completeness. One of the first differential operators encountered in image processing is the gradient, used primarily for edge detection. The gradient of a scalar function I is defined in a coordinate-free fashion in \mathbb{R}^n by imposing that the directional derivative of a scalar field satisfies

$$D_{\mathbf{v}} I = \nabla I \cdot \mathbf{v}.$$

On a Riemannian manifold (\mathcal{M}, g_{ij}) , directional derivatives are replaced by vectors \mathbf{v} in the tangent plane of \mathcal{M} at a point p and the scalar product at p is naturally defined through the metric

$$\mathbf{v}[I] = \langle \nabla I, \mathbf{v} \rangle_p.$$

In a local system of coordinates x^i on \mathcal{M} , the components of the gradient will, thus, read

$$\nabla^i = g^{ij} \frac{\partial}{\partial x^j}. \quad (22)$$

A similar reasoning leads to the expression of the divergence of a vector field \mathbf{X} on \mathcal{M}

$$\text{div} \mathbf{X} = \frac{1}{\sqrt{g}} \partial_i (X^i \sqrt{g})$$

where g is the determinant of g^{ij} . Finally, just as the ordinary Laplacian is defined in \mathbb{R}^n by combining these two operators, the Laplace–Beltrami [6] operator is the second order differential operator defined on scalar fields on \mathcal{M} by

$$\Delta I = -\frac{1}{\sqrt{g}} \partial_j (g^{ij} \sqrt{g} \partial_i I). \quad (23)$$

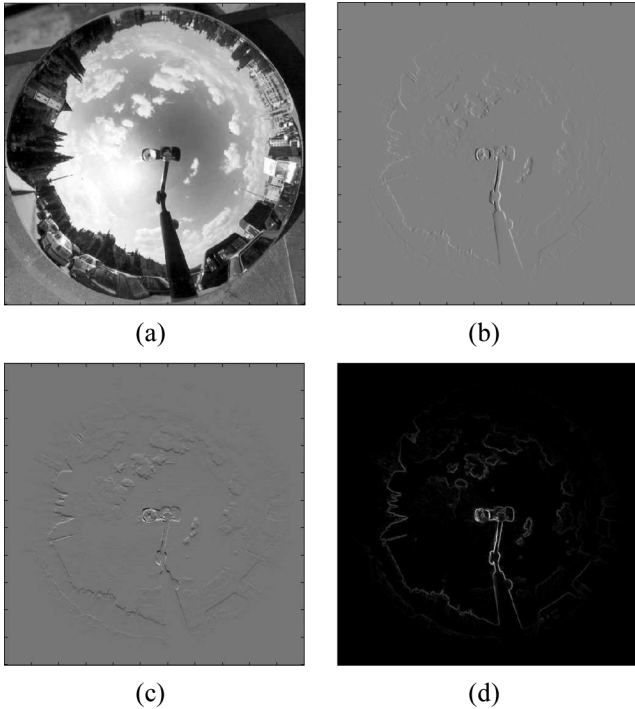


Fig. 6. Gradient of a hyperbolic image: (a) original image, (b) component of the gradient in the horizontal direction, (c) component of the gradient in the vertical direction, and (d) norm of the gradient.

B. Examples

As a first example of the concepts introduced above, let us consider the problem of detecting edges of an omnidirectional image produced by a hyperbolic mirror. As depicted in Section II-B, we approximate the catadioptric system by a stereographic projection and work directly in the open unit disk in \mathbb{R}^2 . The main advantage as we will see is that we can implement most techniques directly in cartesian coordinates from the sensor output while respecting the geometry of the mirror. The induced hyperbolic metric in the disk has been computed in (21) for cartesian coordinates (x, y) . Using (22), and since this metric is conformally equivalent to the euclidean cartesian metric, we see that the hyperbolic gradient is just a scaled version of its usual euclidean cousin

$$\nabla_D = \frac{(1 - (x^2 + y^2))^2}{4} \nabla_{\mathbb{R}^2}.$$

The scaling factor in this expression goes to zero on the border of the disk, which does not belong to the image domain. It is exactly the conformal factor in the hyperbolic metric and governs how the size and morphology of patterns in the image vary. To illustrate its effect, we apply the gradient to localize edges of an omnidirectional image acquired with a hyperbolic mirror in Fig. 6. More precisely, we computed the horizontal and vertical components of the gradient, as well as its norm. Note that, in the latter case, the correct scalar product has been used

$$|\nabla_D I|^2 = h_{i,j} \nabla_D^i I \nabla_D^j I \quad (24)$$

$$= \frac{(1 - (x^2 + y^2))^2}{4} |\nabla_{\mathbb{R}^2} I|^2. \quad (25)$$

As a second example, we would like to illustrate how one can easily implement gaussian smoothing or, equivalently, linear scale-space [7]–[9]. We will keep this discussion general enough so that it can be applied to problems other than omnidirectional computer vision. There are two popular ways of computing gaussian filtering in euclidean computer vision: either using convolution with a gaussian kernel or by implementing the linear heat flow. On general manifolds, though, the situation becomes trickier. First, gaussian filtering may simply not exist: on the paraboloid for example, there is no clear notion of Fourier analysis or convolution theorem. In fact, these mathematical constructions make sense on homogeneous spaces of Lie groups, such as the sphere or the hyperboloid. However, even in these nicer cases, the situation is not so simple. Indeed, if filtering can be easily implemented on S^2 thanks to a spherical equivalent of the fast Fourier transform [10], it is not the case on H^2 : there is a convolution and a Fourier transform (the Helgason transform; see [11]), but there is no efficient algorithm and naive implementations based on separation of variables cannot be applied since the Helgason kernel is not separable. One has to resort to more involved numerical schemes [12], [13]. The best way to compute gaussian filtering on manifolds is, thus, to use the linear heat flow

$$\frac{\partial}{\partial t} I(\mathbf{x}, t) = \Delta I(\mathbf{x}, t) \quad (26)$$

where Δ is the Laplace–Beltrami operator. Then again, implementing PDEs on manifolds may be quite complicated: usually differential operators are expressed in local coordinate systems which are hard to handle numerically.

In [14] and [15], the authors introduced a new framework for solving variational problems and PDEs for scalar and vector-valued data defined on arbitrary surfaces implicitly represented by a level set function (see also [16], [17], and references therein). Level set functions are basically defined on a fixed cartesian coordinate system, which allows easy computations of PDEs on level set-based surfaces contrary to surfaces represented by triangulated models. The main advantage of the previous framework is to carry out, e.g., the linear heat flow on *arbitrary* surfaces even if the method requires to use a data extension procedure from the surface to a cartesian narrow band. It is, however, not clear what the exact extension procedure is. There are different models to extend data and one natural and fast method is to extend data in such a way that they are constant normal to each level set [18]. In our case of omnidirectional images, a *global parametrization* of surfaces is available, which allows to map the surface and its geometry to an euclidean parametric base. We, thus, propose to simply compute the heat flow on that base, which only requires cartesian differential operators, and then eventually map the result to the original surface. This approach provides fast and exact computations of the linear scale space without using a level set function or a triangulated surface but is limited to parametric surfaces.

Let us once again illustrate this mechanism with the hyperboloid. A scalar image painted on H^2 is first mapped to the open unit disk by stereographic projection. The Escher painting

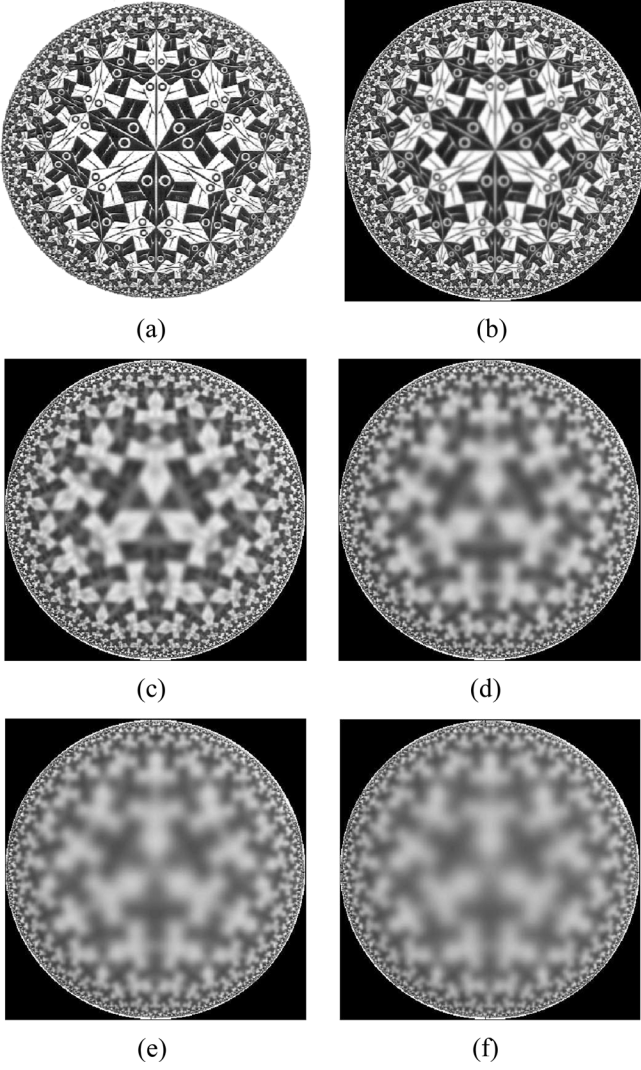


Fig. 7. Heat flow/Gaussian smoothing on a hyperbolic image: (a) original, (b) $t = 10$, (c) $t = 100$, (d) $t = 300$, (e) $t = 500$, and (f) $t = 700$. Note how the flow is comparatively slower close to the border of the disk.

in Fig. 7 is a good example of such an image. The only thing we need to compute the heat flow, is the expression of the Laplace–Beltrami operator in the unit disk, given the metric (21)

$$\begin{aligned}
 \Delta_{D_+} I &= \frac{1}{\sqrt{h}} \left(\frac{\partial}{\partial x} \sqrt{h} h^{xx} \frac{\partial I}{\partial x} + \frac{\partial}{\partial y} \sqrt{h} h^{yy} \frac{\partial I}{\partial y} \right) \\
 &= \frac{(1 - x^2 - y^2)^2}{4} \left(\frac{\partial^2 I}{\partial x^2} + \frac{\partial^2 I}{\partial y^2} \right) \\
 &= \frac{(1 - x^2 - y^2)^2}{4} \Delta_{\mathbb{R}^2} I.
 \end{aligned} \tag{27}$$

Once again, conformal equivalence has reduced this expression to a scaling factor times the usual Laplacian in \mathbb{R}^2 . Implementation is, thus, trivial and requires only an efficient discrete Laplacian [19]. The action of the Laplace–Beltrami heat flow in the disk is illustrated in Fig. 7 for various evolution times t . As one can notice, the flow behaves like a linear euclidean heat flow only close to the origin. As one moves closer to the border of the disk, the scaling factor in (27) slows the flow down. This can

also be understood intuitively as the size of patterns close to the border of the disk is actually much bigger than measured with euclidean tools. It will, thus, take more time to smooth them out of the image.

Deriving the gradient and Laplace–Beltrami operators was very simple in the case of H^2 thanks to conformal equivalence. The same of course holds true for the sphere. The case of the paraboloid is slightly more complicated but involves only straightforward applications of the definitions. For example, the Laplace–Beltrami operator computed with the metric (8) reads

$$\begin{aligned}
 \Delta_{P^2} = & - \frac{1}{1 + 4x^2 + 4y^2} \\
 & \times \left[(1 + 4y^2) \frac{\partial^2 I}{\partial x^2} - 4xy \frac{\partial^2 I}{\partial x \partial y} + (1 + 4x^2) \right. \\
 & \times \frac{\partial^2 I}{\partial y^2} - \frac{8x(1 + 2x^2 + 2y^2)}{(1 + 4x^2 + 4y^2)} \frac{\partial I}{\partial x} \\
 & \left. - \frac{8y(1 + 2x^2 + 2y^2)}{(1 + 4x^2 + 4y^2)} \frac{\partial I}{\partial y} \right].
 \end{aligned}$$

IV. SEGMENTATION WITH ACTIVE CONTOURS ON OMNIDIRECTIONAL IMAGES

In this section, we define the evolution equation of geodesic active contours tailored to omnidirectional images. We start by considering spherical and hyperbolic geometry, where conformal equivalence makes it easy to alter the initial theory. We then describe a broader technique that is able to cope with a larger class of manifolds, including the paraboloid.

A. Active Contour on Conformally Euclidean Surfaces

Geodesic active contours (GAC) were introduced by Caselles *et al.* in [2] and Kichenassamy *et al.* in [20] to overcome the limitations of traditional snakes. They are defined as minimizers of following energy:

$$\begin{aligned}
 F_{\text{GAC}}(C) &= \int_0^1 f(|\nabla I_0(C(p))|) |C_p| dp \\
 &= \int_0^{L(C)} f(|\nabla I_0(C(s))|) ds
 \end{aligned} \tag{28}$$

where $C : [0, 1] \mapsto \mathbb{R}^2$ is a closed planar curve, C_p its first derivative with respect to the parameter p , $L(C)$ is the Euclidean length of C , I_0 is a given image, represented here as a positive bounded function and f is an edge detector function. It was proved in [2] that the direction for which F_{GAC} decreases most rapidly provides the following minimization flow:

$$\frac{\partial C}{\partial t} = (\kappa f - \langle \nabla f, \mathcal{N} \rangle) \mathcal{N} \tag{29}$$

where \mathcal{N} is the unit normal to the curve C and κ is its curvature. The right hand side of the (29) corresponds to the Euler–Lagrange of energy (28). The first term is the mean curvature motion, also called curve shortening flow, weighted by the edge detector function f . It smoothes the curve shape by decreasing

its total length as fast as possible. The second term of (29) attracts the curve toward the boundaries of objects by creating an attraction valley centered on the edges. Hence, the function f does not need to be equal to zero to stop the evolution of the snake on the contours of objects.

In [2], Caselles *et al.* proved that the curve minimizing $F_{\text{GAC}}(C)$ is actually a geodesic in a Riemannian space whose metric tensor is

$$a_{ij} = f^2 (|\nabla I_0|) \delta_{ij} \quad (30)$$

where δ_{ij} is the Euclidean metric tensor. This fact is proved by considering the general definition of a geodesic, i.e., a curve of minimal weighted distance/length between two points on a given Riemannian space. The minimal length between two points on a manifold equipped with the metric tensor a_{ij} is given by the following standard formula:

$$\int_0^1 \sqrt{a_{ij} C_p^i C_p^j} dp = \int_0^1 \sqrt{a_{11} (C_p^1)^2 + 2a_{12} C_p^1 C_p^2 + a_{22} (C_p^2)^2} dp$$

with $C = (C^1, C^2)$ and $C_p^i := \partial C^i / \partial p$. Considering the metric (30), the active contour energy can be expressed in an equivalent way

$$\begin{aligned} F_{\text{GAC}}(C) &= \int_0^1 f (|\nabla I_0(C(p))|) |C_p| dp \\ &= \int_0^1 f (|\nabla I_0(C(p))|) \sqrt{\delta_{ij} C_p^i C_p^j} dp \\ &= \int_0^1 \sqrt{f^2 (|\nabla I_0(C(p))|) \delta_{ij} C_p^i C_p^j} dp. \end{aligned} \quad (31)$$

This formalism encodes the geometry of edges in the new metric, but we see from (31) that the geometry of the evolving curve is still Euclidean. When the active contour C evolves in a more general space, defined by the first fundamental form h_{ij} , we, thus, propose to modify the formalism to take geometry into account. The most obvious modification is to simply introduce the correct metric and this leads to a new energy functional

$$\int_0^1 f (|\nabla I_0(C(p))|) \sqrt{h_{ij} C_p^i C_p^j} dp \quad (32)$$

which reduces to the standard active contour model when the metric $h_{ij} = \delta_{ij}$, i.e., the Euclidean metric.

Let us now go back to the specific case of omnidirectional images. The metric tensor for the sphere and the hyperboloid, defined in (14) and (21), are both conformally equivalent to the Euclidean metric through stereographic projection. This allows us to simplify Functional (32) considering $h_{ij} = h^{1/2} \delta_{ij}$ where

h is the determinant of h_{ij} . Inserting this expression into (32), we get

$$\begin{aligned} &\int_0^1 \underbrace{f (|\nabla I_0(C(p))|) h^{1/4}(C(p))}_{=: f_D(C(p))} \sqrt{\delta_{ij} C_p^i C_p^j} dp \\ &= \int_0^1 f_D(C(p)) |C_p| dp = F_{\text{ACSHM}}(C) \end{aligned} \quad (33)$$

which corresponds to the energy of active contours on either spherical or hyperbolic manifolds (ACSHM) and f_D (D stands for disk) is the edge detector function for either the spherical or the hyperbolic (non-Euclidean) images. The evolution equation of the curve C minimizing energy (33) is naturally obtained by replacing the function f by f_D in (29)

$$\begin{aligned} \frac{\partial C}{\partial t} &= (\kappa f_D - \langle \nabla f_D, \mathcal{N} \rangle) \mathcal{N} \\ &= \left(\kappa f h^{1/4} - \langle \nabla (f h^{1/4}), \mathcal{N} \rangle \right) \mathcal{N}. \end{aligned} \quad (34)$$

We notice that (34) is defined on the planar open domain D , which corresponds to the stereographic projection of the sphere and the hyperboloid onto the plane (see Section II-A and B). Thus, the evolution equation of the active contour is not directly performed on the spherical or the hyperbolic manifold but on the plane by taking into account the geometry of the given manifolds with the factor $h^{1/4}$. Then the snake is mapped onto the sphere and the hyperboloid with a one-to-one mapping defined in Section II-A and B. This way of evolving the active contour on nonflat spaces, whose metric tensors are known, is, thus, very fast and numerically accurate. It does require a global parametrization and, so far, conformal equivalence with \mathbb{R}^2 . In the next section, we will consider a larger class of manifolds.

Let us now consider two examples of illustration of these new active contour models. The first example presents the evolution of the snake on the hyperbolic manifold by the mean curvature flow, Figs. 8 and 9. The geometry of the hyperboloid is defined by the metric tensor in (21), which implies that $h^{1/4} = (2/|1 - (x^2 + y^2)|)$. The mapping between the disk D , which corresponds to the stereographic projection of the hyperboloid onto the plane, is given by

$$\begin{aligned} (x, y) \in D &\rightarrow (x_{H_+^2}, y_{H_+^2}, z_{H_+^2}) \\ &= (\sinh \chi \cos \varphi, \sinh \chi \sin \varphi, \cosh \chi) \in H_+^2 \end{aligned} \quad (35)$$

given

$$(\chi, \varphi) = \left(2 \tanh^{-1} \left(\frac{1}{2} \sqrt{x^2 + y^2} \right), \tan^{-1} \left(\frac{y}{x} \right) \right).$$

The second example carries out the image segmentation task on the sphere by extracting Australia, Fig. 11. The metric tensor of the sphere is defined in (14), which implies that $h^{1/4} = 2/|1 + x^2 + y^2|$. Besides, the mapping between the plane $\Omega_{\theta, \varphi}$ of

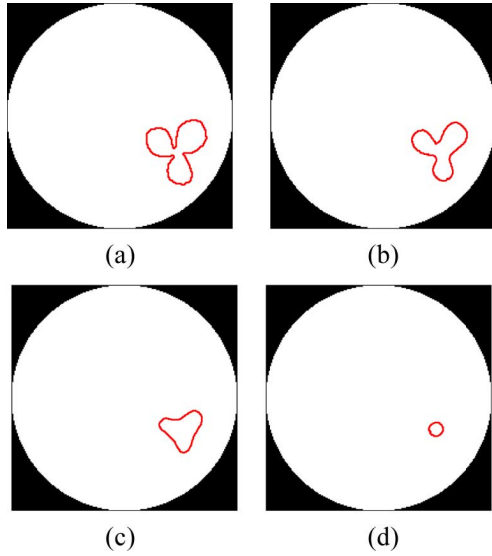


Fig. 8. Mean curvature flow on the hyperboloid; (a)–(d) present the evolution of the AC on the disk D given by (34) when $f = 1$. The disk D corresponds to the stereographic projection of the hyperboloid onto the plane. (a) Initial AC on D ; (b) AC at $t_1 > 0$; (c) AC at $t_2 > t_1$; (d) AC at $t_3 > t_2$.

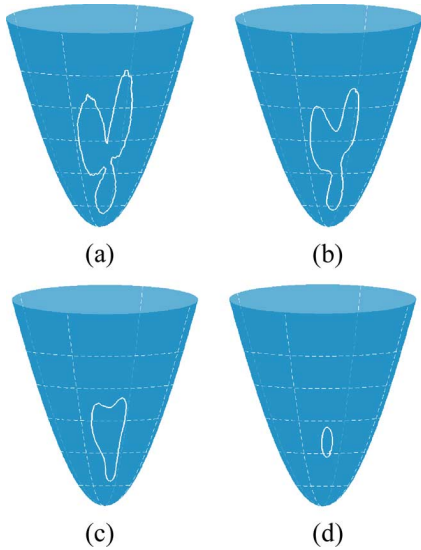


Fig. 9. Mean curvature flow on the hyperboloid; (a)–(d) shows the evolution of the AC of Fig. 8 on the hyperboloid H_+^2 when using the mapping from the disk to the hyperboloid defined in (35). (a) Initial AC on H_+^2 ; (b) AC at $t_1 > 0$; (c) AC at $t_2 > t_1$; (d) AC at $t_3 > t_2$.

(θ, φ) -values, given in Fig. 10(a), and the disk D in Fig. 10(b), which corresponds to the stereographic projection of the sphere onto the plane, is given by

$$(\theta, \varphi) \in \Omega_{\theta, \varphi} \rightarrow (x, y) = \left(2 \tan \frac{\theta}{2} \cos \varphi, 2 \tan \frac{\theta}{2} \sin \varphi \right) \in D$$

and the mapping between the disk and the sphere S^2 is given by

$$\begin{aligned} (x, y) \in D &\rightarrow (x_{S^2}, y_{S^2}, z_{S^2}) \\ &= (\cos \theta, \sin \theta \cos \varphi, \sin \theta \sin \varphi) \in S^2 \end{aligned} \quad (36)$$



Fig. 10. Three equivalent representations of the omnidirectional image *earth* (a) in the parametric (θ, φ) plane and (b) in the disk D using the stereographic projection. (c) Original image as a scalar function on S^2 .

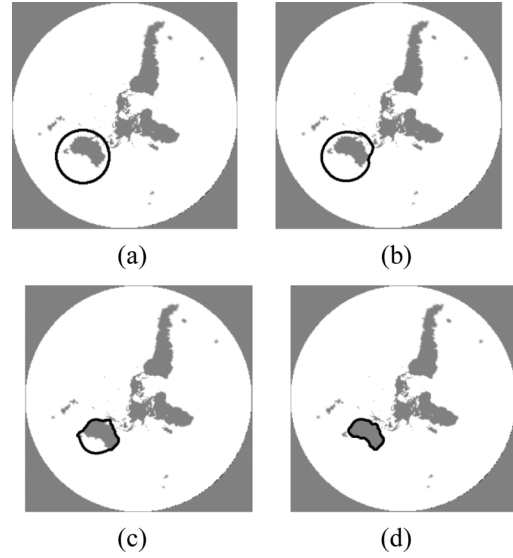


Fig. 11. Segmentation of Australia on the sphere; (a)–(d) present the evolution of the AC on the disk D given by (34). The disk D corresponds to the stereographic projection of the sphere onto the plane. (a) Initial AC on D ; (b) AC at $t_1 > 0$; (c) AC at $t_2 > t_1$; (d) final AC.

given

$$(\theta, \varphi) = \left(2 \tan^{-1} \left(\frac{1}{2} \sqrt{x^2 + y^2} \right), \tan^{-1} \left(\frac{y}{x} \right) \right).$$

The numerical implementation of the minimizing flow (34) is done with standard numerical schemes (see [21] and [22] for details).

B. Active Contours on the Paraboloid

In the previous section, an evolution equation for the active contours on spherical and hyperbolic manifolds was defined from the minimization of Functional (32) using the metric of these manifolds. These metrics have a simple form, $h_{ij} = h^{1/2} \delta_{ij}$, which allows us to directly find the evolution equation for the snake from the standard geodesic/geometric active contours [2], [20]. In this section, we want to derive the evolution equation for the active contours on parabolic manifolds whose metric tensor is defined in (8). In this case, the metric is not diagonal, which implies more developments to find the evolution equation from the minimization of (32). Instead of computing the Euler–Lagrange equation of the functional (32), we propose to apply the formalism defined by Bresson *et al.* in [3] and [23], which consider the general case of an active hypersurface evolving on any given Riemannian

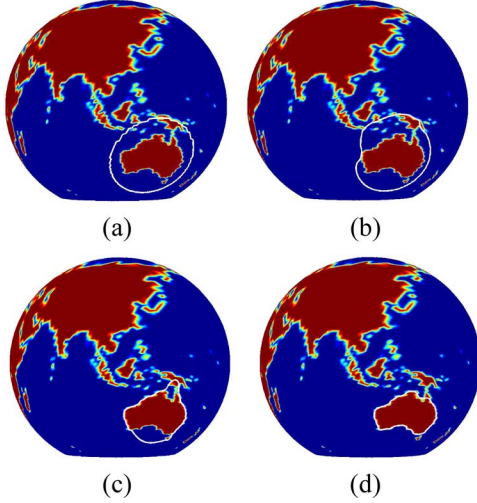


Fig. 12. Segmentation of Australia on the sphere; (a)–(d) show the evolution of the AC of Fig. 11 on the sphere S^2 using the mapping from the disk to the sphere defined in (36). (a) Initial AC on S^2 ; (b) AC at $t_1 > 0$; (c) AC at $t_2 > t_1$; (d) final AC.

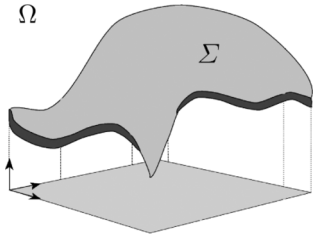


Fig. 13. Manifold Σ embedded in Ω , reproduced from [24].

manifold. This formalism is based on the work of Sochen *et al.* [24] and [25], who introduced the Beltrami framework. The Beltrami framework is a differential geometric framework for image processing, which represents images as Riemannian manifolds embedded in a higher dimensional Riemannian manifold. The Beltrami flow applied on images determines a minimal hyper-surface which exhibits very nice geometric properties such as smoothing images while preserving edges. In [3] and [23], authors used the Beltrami framework to generalize the model of active contours. In their approach, they replaced the embedding manifold (which is the given image in [24] and [25]) by an active contour, which is embedded in a higher dimensional Riemannian manifold (as the given image in [24] and [25]). In what follows, we first remind the general model introduced in [3] and [23], then we focus the model to a contour embedded in a parabolic manifold.

We consider the following functional introduced in [3] and [23]

$$\begin{cases} P_f(X, \Sigma, \Omega) \\ = \int d^{n_\Sigma} \varsigma f(X, \sigma_{\mu\nu}, h_{ij}) \sigma^{1/2} \sigma^{\mu\nu} \partial_\mu X^i \partial_\nu X^j h_{ij} \\ X : (\Sigma, \sigma_{\mu\nu}) \rightarrow (\Omega, h_{ij}) \end{cases} \quad (37)$$

which corresponds to the Polyakov action [26] weighted by the function f . The Polyakov action is basically a functional that measures the weight of a mapping X between an embedded manifold Σ and the embedding manifold Ω (see Fig. 13).

More precisely, $\sigma_{\mu\nu}$ is the first fundamental form of the manifold Σ , $\sigma^{\mu\nu}$ is the inverse metric of $\sigma_{\mu\nu}$, σ is the determinant of $\sigma_{\mu\nu}$, n_Σ is the dimension of Σ , $\mu, \nu = 1, \dots, n_\Sigma$, $d^{n_\Sigma} \varsigma \sigma^{1/2}$ is the volume element w.r.t. the local coordinates on Σ , h_{ij} is the metric tensor of the embedding space Ω , n_Ω the dimension of Ω , $i, j = 1, \dots, n_\Omega$, $\partial_\mu X^i = \partial X^i / \partial \varsigma^\mu$, and $\sigma^{\mu\nu} \partial_\mu X^i \partial_\nu X^j h_{ij}$ is the generalization of the magnitude of the gradient to maps between Riemannian manifolds. We observe that the volume element as well as the rest of the expression is re-parametrization invariant. In other words, they are invariant under a smooth transformation. Thus, this action depends on the geometrical objects and not on the way we describe them via our parametrization of the coordinates. Finally, when identical indices appear one up and one down in (37), they are summed over according to the Einstein summation convention.

The calculus of variations gives us the flow minimizing Functional (37) w.r.t. the l th embedding coordinate X^l , $\sigma_{\mu\nu}$ and h_{ij} being fixed

$$\begin{aligned} \frac{\partial X^l}{\partial t} = & f(X, \sigma_{\mu\nu}, h_{ij}) \\ & \cdot \left(\sigma^{-1/2} \partial_\mu (\sigma^{1/2} \sigma^{\mu\nu} \partial_\nu X^l) + \Gamma_{jk}^l \partial_\mu X^j \partial_\nu X^k \sigma^{\mu\nu} \right) \\ & + \partial_k f \sigma^{\mu\nu} \partial_\mu X^k \partial_\nu X^l \\ & - \frac{n_\Omega}{2} h^{lk} \partial_k f \sigma^{\mu\nu} \partial_\mu X^i \partial_\nu X^j h_{ij} \end{aligned} \quad (38)$$

for $1 \leq l \leq n_\Omega$, $g^{-1/2} \partial_\mu (\sigma^{1/2} \sigma^{\mu\nu} \partial_\nu X^l)$ is the Beltrami operator which generalizes the Laplace operator to nonflat manifolds and $\Gamma_{jk}^l = (1/2) h^{li} (\partial_j h_{ik} + \partial_k h_{ji} - \partial_i h_{jk})$ is the Levi-Civita connection coefficients. If the metric tensor $\sigma_{\mu\nu}$ of the embedded manifold Σ is chosen to be the induced metric tensor; $\sigma_{\mu\nu} = \partial_\mu X^i \partial_\nu X^j h_{ij}$, then the map X are harmonic maps such as geodesics and minimal surfaces and the weighted Polyakov action is reduced to the weighted Euler functional/Nambu action that describes the (hyper-)area of a (hyper-)surface Σ

$$S_f = \int d^{n_\Sigma} \varsigma f \sigma^{1/2}. \quad (39)$$

The induced metric tensor is also introduced in the flow (38), which yields to

$$\begin{cases} \frac{\partial X^l}{\partial t} = f \cdot \mathcal{H}^l + \partial_k f \sigma^{\mu\nu} \partial_\mu X^k \partial_\nu X^l - \frac{n_\Omega \cdot n_\Sigma}{2} \partial_k f h^{kl} \\ \mathcal{H}^l = \left(\sigma^{-1/2} \partial_\mu (\sigma^{1/2} \sigma^{\mu\nu} \partial_\nu X^l) \right. \\ \quad \left. + \Gamma_{jk}^l \partial_\mu X^j \partial_\nu X^k \sigma^{\mu\nu} \right)_{\sigma_{\mu\nu} = \partial_\mu X^i \partial_\nu X^j h_{ij}} \end{cases} \quad (40)$$

for $1 \leq l \leq n_\Omega$ and \mathcal{H} is the mean curvature vector generalized to any embedding manifold Ω . Thus, the functional (39) and the minimization flow (40) define the energy and the evolution equation for the active contour model defined in a general Riemannian manifold such as hyperbolic, spherical or parabolic manifolds.

The previous model is consistent with the standard geodesic/geometric active contours model [2], [20] when the embedding

manifold is the Euclidean space, i.e., $\Omega = \mathbb{R}^2$, $h_{ij} = \delta_{ij}$. Indeed, let us choose $X = C : p \rightarrow (C^1(p), C^2(p))$, which means that the metric tensor of Σ is as follows:

$$\begin{aligned}\sigma_{\mu\nu} &= \partial_\mu X^i \partial_\nu X^j h_{ij} = \partial_\mu C^i \partial_\nu C^j \delta_{ij} \\ &= |C_p|^2 = \sigma_{pp} = \sigma\end{aligned}$$

with $\mu = \nu = p$. Energy functional (39) is, thus, equal to

$$\int d^{n_\Sigma} \varsigma f \sigma^{1/2} = \int dp f |C_p| = F_{\text{GAC}}(C)$$

which corresponds to the energy of the geodesic/geometric active contour model defined in (28) when f is the edge detector function. The minimization flow (29) can also be recovered. The mean curvature vector is equal to

$$\begin{aligned}\mathcal{H}^l &= \left(\sigma^{-1/2} \partial_\mu (\sigma^{1/2} \sigma^{\mu\nu} \partial_\nu X^l) \right. \\ &\quad \left. + \Gamma_{jk}^l \partial_\mu X^j \partial_\nu X^k \sigma^{\mu\nu} \right)_{\sigma_{\mu\nu} = \partial_\mu X^i \partial_\nu X^j h_{ij}} \\ &= \frac{1}{|C_p|} \partial_p \left(\frac{\partial_p C^l}{|C_p|} \right) = \frac{1}{|C_p|} \partial_p \mathcal{T}^l = \kappa \mathcal{N}^l\end{aligned}$$

using $\mathcal{T} = C_p/|C_p|$ and $\partial_p \mathcal{T} = |C_p| \partial_s \mathcal{T} = |C_p| \kappa \mathcal{N}$. The second part of the flow is equal to

$$\begin{aligned}\partial_k f \sigma^{\mu\nu} \partial_\mu X^k \partial_\nu X^l - \frac{n_{\Omega \cdot n_\Sigma}}{2} \partial_k f h^{kl} \\ &= \frac{1}{|C_p|^2} \partial_k f \cdot \partial_p C^k \partial_p C^l - \partial_k f \delta^{kl} \\ &= \left\langle \nabla f, \frac{C_p}{|C_p|} \right\rangle \frac{C_p^l}{|C_p|} - \partial_l f \\ &= \langle \nabla f, \mathcal{T} \rangle \mathcal{T}^l - \partial_l f = -\langle \nabla f, \mathcal{N}^l \rangle \mathcal{N}^l.\end{aligned}$$

Finally, the flow (40) is as follows:

$$\partial_t C = f \kappa \mathcal{N} - \langle \nabla f, \mathcal{N} \rangle \mathcal{N} \quad (41)$$

which is exactly the flow of the geodesic/geometric active contour model defined in (29).

We now determine the energy and the evolution equation for the active contours evolving on parabolic manifolds. We remind the metric tensor for a parabolic manifold, defined in (8)

$$(h_{ij})_{P^2} = \begin{pmatrix} 1 + 4x^2 & 4xy \\ 4xy & 1 + 4y^2 \end{pmatrix}$$

and the inverse tensor is as follows:

$$(h^{ij})_{P^2} = h^{-1} \begin{pmatrix} 1 + 4y^2 & -4xy \\ -4xy & 1 + 4x^2 \end{pmatrix}$$

where $h = 1 + 4x^2 + 4y^2$ is the determinant of h_{ij} . The metric tensor of the active contour, $\Sigma = C$ in the Polyakov framework, embedded on a parabolic manifold, $\Omega = P^2$, is as follows:

$$\begin{aligned}\sigma_{\mu\nu} &= \partial_\mu X^i \partial_\nu X^j h_{ij} = \partial_p C^i \partial_p C^j h_{ij} \\ &= |C_p|^2 \left(\frac{C_p^1}{|C_p|} \frac{C_p^1}{|C_p|} h_{xx} + 2 \frac{C_p^1}{|C_p|} \frac{C_p^2}{|C_p|} h_{xy} + \frac{C_p^2}{|C_p|} \frac{C_p^2}{|C_p|} h_{yy} \right) \\ &= |C_p|^2 (T^1 T^1 h_{xx} + 2 T^1 T^2 h_{xy} + T^2 T^2 h_{yy}) \\ &= |C_p|^2 T^T (h_{ij})_{P^2} T = |C_p|^2 |T|_{P^2} = \sigma_{pp} = \sigma\end{aligned}$$

where T^T means the transpose of T and $|T|_{P^2}$ is the norm of the tangent vector on the parabolic manifold. Thus, energy

functional (39) of the active contours embedded on a parabolic manifold is equal to

$$\begin{aligned}\int d^{n_\Sigma} \varsigma f \sigma^{1/2} &= \int f |T|_{P^2} |C_p| dp \\ &= \int f |T|_{P^2} ds = F_{\text{ACPM}}(C)\end{aligned}$$

where ACPM stands for active contours on parabolic manifolds. Let us now compute the evolution equation for the active contours on a parabolic manifold. The Beltrami part is equal to

$$\begin{aligned}\sigma^{-1/2} \partial_\mu (\sigma^{1/2} \sigma^{\mu\nu} \partial_\nu X^l) &= \sigma^{-1/2} \partial_p \left(\sigma^{-1/2} |C_p| \frac{\partial_p C^l}{|C_p|} \right) \\ &= \sigma^{-1} |C_p|^2 \kappa \mathcal{N}^l \\ &\quad - \frac{1}{2} \sigma^{-2} |C_p|^2 \langle \nabla \sigma, \mathcal{T} \rangle \mathcal{T}^l.\end{aligned}$$

The Levi-Civita connection coefficients are equal to

$$\begin{aligned}\Gamma_{jk}^l &= \frac{1}{2} h^{li} (\partial_j h_{ik} + \partial_k h_{ji} - \partial_i h_{jk}) \\ \Gamma_{jk}^1 &= 4h^{-1} x \delta_{jk} \\ \Gamma_{jk}^2 &= 4h^{-1} y \delta_{jk}\end{aligned}$$

which gives us the second term of the mean curvature vector:

$$\begin{aligned}\Gamma_{jk}^1 \partial_p C^j \partial_p C^k \sigma^{pp} &= 4h^{-1} x \delta_{jk} \partial_p C^j \partial_p C^k \sigma^{-1} \\ &= 4h^{-1} \sigma^{-1} |C_p|^2 x \\ \Gamma_{jk}^2 \partial_p C^j \partial_p C^k \sigma^{pp} &= 4h^{-1} y \delta_{jk} \partial_p C^j \partial_p C^k \sigma^{-1} \\ &= 4h^{-1} \sigma^{-1} |C_p|^2 y\end{aligned}$$

which is as follows under the vectorial form:

$$\Gamma_{jk} \partial_\mu X^j \partial_\nu X^k \sigma^{\mu\nu} = 4h^{-1} \sigma^{-1} |C_p|^2 \mathbf{x} \quad (42)$$

where $\mathbf{x} = (x, y)$. Thus, the mean curvature vector is equal to

$$\begin{aligned}\mathcal{H} &= \left(\sigma^{-1/2} \partial_\mu (\sigma^{1/2} \sigma^{\mu\nu} \partial_\nu X) \right. \\ &\quad \left. + \Gamma_{jk} \partial_\mu X^j \partial_\nu X^k \sigma^{\mu\nu} \right)_{\sigma_{\mu\nu} = \partial_\mu X^i \partial_\nu X^j h_{ij}} \\ &= \sigma^{-1} |C_p|^2 \kappa \mathcal{N} - \frac{1}{2} \sigma^{-2} |C_p|^2 \langle \nabla \sigma, \mathcal{T} \rangle \mathcal{T} \\ &\quad + 4h^{-1} \sigma^{-1} |C_p|^2 \mathbf{x}.\end{aligned}$$

Then, the second part of the flow (40) is equal to

$$\begin{aligned}\partial_k f \sigma^{\mu\nu} \partial_\mu X^k \partial_\nu X^l &= \partial_k f \sigma^{pp} \partial_p C^k \partial_p C^l \\ &= \sigma^{-1} |C_p|^2 \langle \nabla f, \mathcal{T} \rangle \mathcal{T}^l\end{aligned}$$

and the term $-(n_{\Omega \cdot n_\Sigma}/2) \partial_k f h^{kl}$ is equal for $l = 1, 2$ to

$$\begin{aligned}- \left(\partial_x f h^{xx} + \partial_y f h^{xy} \right) &= - \begin{pmatrix} h^{xx} & h^{xy} \\ h^{xy} & h^{yy} \end{pmatrix} \begin{pmatrix} \partial_x f \\ \partial_y f \end{pmatrix} \\ &= - (h^{ij}) \nabla f = -\nabla^{P^2} f\end{aligned}$$

where ∇^{P^2} is the gradient operator defined on the manifold P^2 . Finally, the flow (40) for the active contours embedded on a parabolic manifold is as follows:

$$\begin{aligned}\partial_t C &= f \cdot \left[\sigma^{-1} |C_p|^2 \kappa \mathcal{N} - \frac{1}{2} \sigma^{-2} |C_p|^2 \langle \nabla \sigma, \mathcal{T} \rangle \mathcal{T} \right. \\ &\quad \left. + 4h^{-1} \sigma^{-1} |C_p|^2 \mathbf{x} \right] + \sigma^{-1} |C_p|^2 \langle \nabla f, \mathcal{T} \rangle \mathcal{T} - \nabla^{P^2} f.\end{aligned} \quad (43)$$

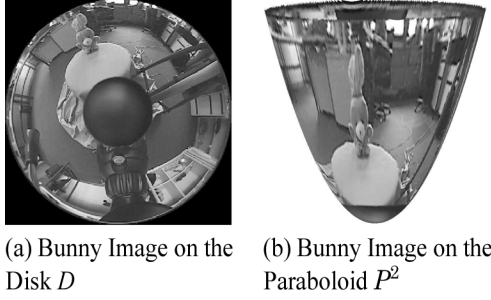


Fig. 14. Original *bunny* image obtained from a catadioptric system. (a) Raw image from the sensor. (b) Omnidirectional image represented as a scalar function on the paraboloid.

In [27], Epstein–Gage proved that the geometry of the curve deformation is not affected by the tangential velocity \mathcal{T} . This result is due to the fact that the tangential velocity does not change the geometry of the curve but its parametrization. Hence, (43) can be replaced by

$$\partial_t C = \sigma^{-1} |C_p|^2 (f\kappa + 4h^{-1} \langle \mathbf{x}, \mathcal{N} \rangle) \mathcal{N} - \langle \nabla^{P^2} f, \mathcal{N} \rangle \mathcal{N}.$$

Since the minimization solution is not changed when the Euler–Lagrange equation is multiplied by a strictly positive function, we finally get the evolution of the active contour on a parabolic manifold

$$\partial_t C = \left(f\kappa - |\mathcal{T}|_{P^2} \langle \nabla^{P^2} f, \mathcal{N} \rangle + 4h^{-1} \langle \mathbf{x}, \mathcal{N} \rangle \right) \mathcal{N} \quad (44)$$

using $\sigma |C_p|^{-2} = |\mathcal{T}|_{P^2}$.

As an example of illustration, we consider the segmentation of the bunny object lying on the parabolic manifold in Figs. 15 and 16. The mapping between the disk D in Fig. 14(a) and the paraboloid, which corresponds to the focal projection of the paraboloid onto the plane, is given by

$$(x, y) \in D \rightarrow (x_{P^2}, y_{P^2}, z_{P^2}) = (r \cos \varphi, r \sin \varphi, r^2) \in P^2 \quad (45)$$

given

$$(r, \varphi) = \left(\sqrt{x^2 + y^2}, \tan^{-1} \left(\frac{y}{x} \right) \right).$$

The numerical implementation of the minimizing flow (44) is done with standard numerical schemes, see [21] and [22] for details.

C. Insightful Example

Previous sections defined evolution equations for active contours evolving on different manifolds. We remind that our basic idea consists in evolving the snake on the disk using the geometry of the given manifold and map the evolving contour on the manifold. However, is it really useful to include the manifold's geometry in the evolution process? In other words, why not just using the standard Euclidean active contour model [2], [20] on the disk and map the evolving contour to the manifold? We introduce here an example to show the importance of taking into

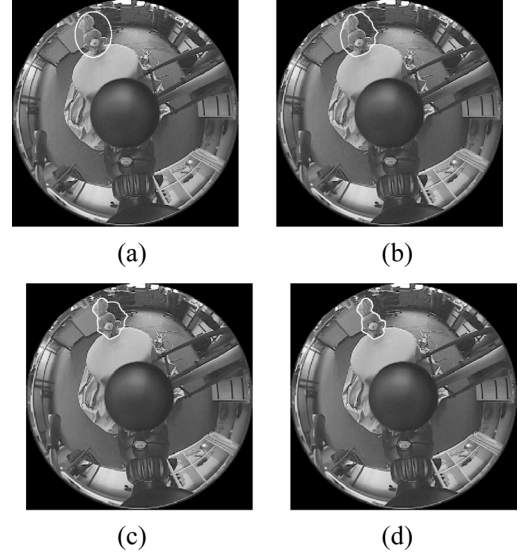


Fig. 15. Segmentation of bunny on the paraboloid; (a)–(d) present the evolution of the AC on the disk D given by (44). The disk D corresponds to the focal projection of the paraboloid onto the plane. (a) Initial AC on D ; (b) AC at $t_1 > 0$; (c) AC at $t_2 > t_1$; (d) final AC.

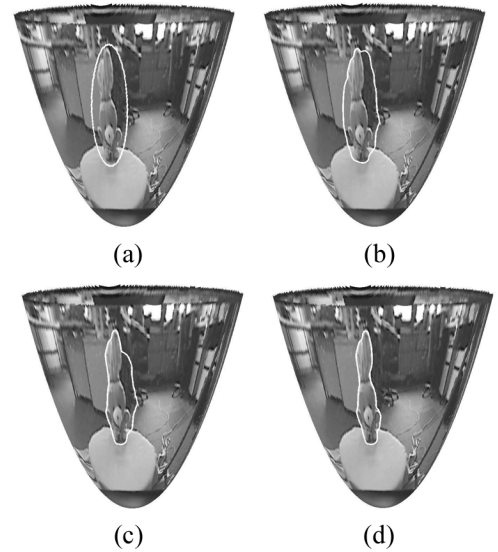


Fig. 16. Segmentation of bunny on the paraboloid. (h)–(k) show the evolution of the AC of Fig. 15 on the paraboloid P^2 using the mapping from the disk to the paraboloid defined in (45). (a) Initial AC on S^2 ; (b) AC at $t_1 > 0$; (c) AC at $t_2 > t_1$; (d) final AC.

account the geometry of the given manifold in the segmentation process. Fig. 17(a) shows an object of interest defined on the hyperbolic manifold. This object presents a smooth transition on the hyperboloid manifold, as one can see in Fig. 17(b), which obviously does not correspond to an edge. However, the projection of this smooth part on the plane, Fig. 17(c), shows a sharp transition corresponding to an edge on the plane. This “false edge” can give unsatisfactory segmentation results if the hyperboloid geometry is not considered. Results based on the Euclidean geometry and the hyperbolic geometry are presented

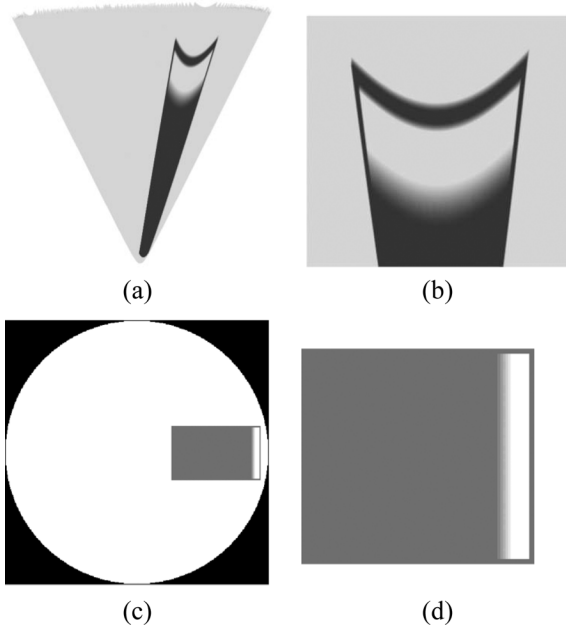


Fig. 17. (a), (b) Object of interest, composed of a smooth transition, painted on the hyperbolic manifold; (c), (d) projection of the object on the plane. The smooth part of the signal on the hyperboloid corresponds to a sharp transition on the plane. (a) Original image on the hyperboloid. (b) Zoom on the object of interest. (c) Original image on the disk. (d) Zoom on the object of interest.

in Figs. 18 and 19. Fig. 18(a)–(h) shows the Euclidean active contour which fails to segment the whole object on the hyperboloid due to the false edge on the disk that corresponds to a smooth transition on the hyperboloid. Fig. 18(i)–(p) presents the hyperbolic active contour that succeeds capturing the entire object because the snake takes into account the geometry of the hyperboloid manifold, which multiplies the edge detector function by a factor $|1 - r^2|/2$, in its evolution.

D. Discussion With Related Works

As we said in Section III, Bertalmio *et al.* in [14], [15] introduced a new framework for solving PDEs on arbitrary surfaces implicitly represented by a level set function. The main advantage of their approach is to deal with arbitrary surfaces, which is not our case, even if a data extension process is needed and the computational time is more important than our technique. In our framework, surfaces are given by a global parametrization, which allows accurate and fast computations of the active contour flows. In [16], [17], and [28], Spira and Kimmel defined the evolution equation of the geodesic active contour on global parametric manifolds by considering the Riemannian counterparts of the Euclidean flow [2]. Our approach is closely related to theirs because we also consider parametric manifolds. However, the main difference lies in the fact that we have developed the flow for the active contours defined on parametric manifolds from a variational model based on the weighted Polyakov functional, which gives the energy of the active contours and the weighted Riemannian length of contours.

V. CONCLUSION

Omnidirectional imaging holds interesting promises for applications and will certainly become a conventional technique

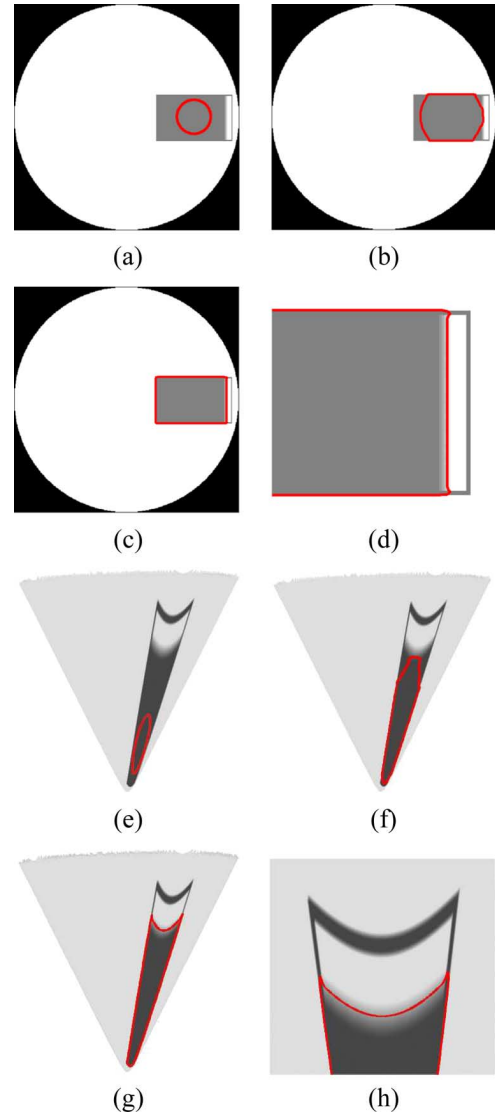


Fig. 18. Segmentation of a synthetic object on the hyperboloid with the *standard* active contour model. (a)–(d) Standard Euclidean active contour (AC) fails to segment the whole object on the hyperboloid due to a false edge on the disk, (e)–(h) corresponding to a smooth transition on the hyperboloid. (a) Euclidean AC on the disk at $t_1 = 0$. (b) Euclidean AC at $t_2 > t_1$. (c) Euclidean AC at $t_3 > t_2$. (d) Zoom on the AC at t_3 . (e) Euclidean AC on the hyperboloid at $t_1 = 0$. (f) Euclidean AC at $t_2 > t_1$. (g) Euclidean AC at $t_3 > t_2$. (h) Zoom on the AC at t_3 .

in the near future. Due to their (eventually near) full covering of the field of view, omnidirectional images allow to monitor a complete scene using a single frame and, thus, provide a very appealing basis for many computer vision algorithms. Manufacturing perfect omnidirectional image acquisition systems seems to be very challenging, but several groups have reported interesting progress [5]. A very interesting and promising research direction is to investigate the properties of insect or animal eyes to design more effective optical devices [29], [30]. Before a new generation of full field of view optical devices matures, the conventional way of acquiring omnidirectional images is through a standard catadioptric setting, where a standard sensor overlooks a curved mirror. The images obtained by such a device are strongly influenced by the geometry of the mirror.

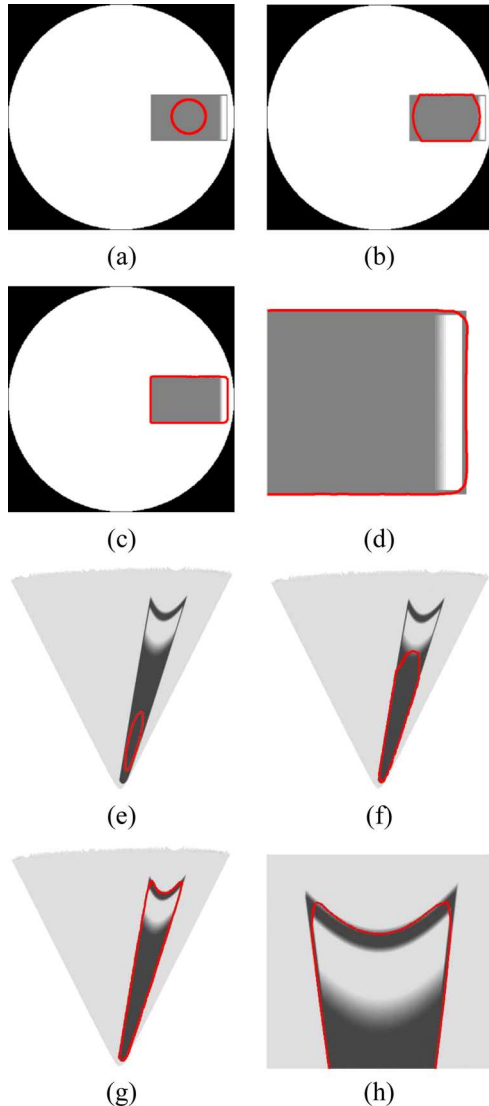


Fig. 19. Segmentation of a synthetic object on the hyperboloid with the proposed active contour model. Hyperbolic active contour (AC) succeeds capturing the entire object, whereas the Euclidean model failed in Fig. 18 because the proposed AC takes into account the geometry of the hyperbolic manifold in its evolution. (a) Hyperbolic AC on the disk at $t_1 = 0$. (b) Hyperbolic AC at $t_2 > t_1$. (c) Hyperbolic AC at $t_3 > t_2$. (d) Zoom on the AC at t_3 . (e) Hyperbolic AC on the hyperboloid at $t_1 = 0$. (f) Hyperbolic AC at $t_2 > t_1$. (g) Hyperbolic AC at $t_3 > t_2$. (h) Zoom on the AC at t_3 .

In this paper, we showed that the output of a catadioptric system can be seen as a scalar function on a special riemannian surface whose metric can be explicitly computed from parameters of the system. We showed that it is important to take these geometric effects into account when using such images for computer vision and methods based on partial differential equations offer the necessary flexibility. First, we derived explicit expressions for standard differential operators used for smoothing or edge detection. Then, we introduced new energy functionals suited for solving segmentation problems on catadioptric images and solved for curve evolution equations using standard calculus of variations. The obtained geometric active contours are appealing because they are able to deal with some of the apparent distortions that plague omnidirectional images. Moreover, for the class of riemannian surfaces studied in this paper,

computations involve only standard euclidean finite differences on the image plane, which means we work directly with sensor pixels.

In a more general perspective, performing smoothing or solving segmentation problems on arbitrary manifolds is a challenge of significant importance for processing large higher dimensional data sets. For example, emerging bioimaging techniques easily acquire 3-D time varying images that need to be automatically segmented [31]. Extending the framework based on the Polyakov action introduced in Section IV could be an interesting way to leverage our results to a much more general case and will be the main topic of a forthcoming paper.

REFERENCES

- [1] C. Geyer and K. Daniilidis, "Catadioptric projective geometry," *Int. J. Comput. Vis.*, vol. 45, no. 3, pp. 223–243, 2001.
- [2] V. Caselles, R. Kimmel, and G. Sapiro, "Geodesic active contours," *Int. J. Comput. Vis.*, vol. 22, no. 1, pp. 61–79, 1997.
- [3] X. Bresson, P. Vandergheynst, and J.-P. Thiran, "Multiscale active contours," *Int. J. Comput. Vis.*, vol. 70, no. 3, pp. 197–211, 2006.
- [4] M. Do Carmo, *Riemannian Geometry*. Cambridge, MA: Birkhauser, 1992.
- [5] J. Neumann, C. Fermüller, and Y. Aloimonos, "Eyes from eyes: New cameras for structure from motion," in *Proc. 3rd Workshop on Omnidirectional Vision*, Jun. 2002, pp. 19–26.
- [6] S. Rosenberg, *The Laplacian on a Riemannian Manifold*. Cambridge, MA: Cambridge Univ. Press, 1997.
- [7] L. Florack, B. ter Haar Romeny, J. Koenderink, and A. Viergever, "Linear scale-space," *J. Math. Imag. Vis.*, vol. 4, no. 4, pp. 225–251, 1994.
- [8] A. P. Witkin, "Scale-space filtering," in *Proc. Int. Joint Conf. Artificial Intelligence*, 1983, pp. 1019–1021.
- [9] T. Lindeberg, *Scale-Space Theory in Computer Vision*. Amsterdam, The Netherlands: Kluwer, 1994.
- [10] D. Healy, D. Rockmore, P. Kostelec, and S. Moore, "FFts for the 2-sphere—Improvements and variations," *J. Fourier Anal. Appl.*, vol. 9, no. 4, pp. 341–385, 2003.
- [11] I. Bogdanova, P. Vandergheynst, and J.-P. Gazeau, "Continuous wavelet transform on the hyperboloid," *Appl. Comput. Harmon. Anal.*, Jun. 2005, submitted for publication.
- [12] A. Spira, R. Kimmel, and N. Sochen, "Efficient beltrami flow using a short time kernel," *Scale Space*, pp. 511–522, Jun. 2003.
- [13] A. Spira, R. Kimmel, and N. Sochen, "A short time Beltrami kernel for smoothing images and manifolds," *IEEE Trans. Image Process.*, vol. 16, no. 6, pp. 1628–1636, Jun. 2007.
- [14] M. Bertalmio, L.-T. Cheng, S. Osher, and G. Sapiro, "Variational problems and partial differential equations on implicit surfaces," *J. Comput. Phys.*, vol. 174, no. 2, pp. 759–780, 2001.
- [15] M. Bertalmio, F. Mémoi, L.-T. Cheng, G. Sapiro, and S. Osher, "Variational problems and partial differential equations on implicit surfaces: Bye bye triangulated surfaces?," in *Geometric Level Set Methods in Imaging, Vision and Graphics*, S. Osher and N. Paragios, Eds. New York: Springer-Verlag, 2003, pp. 381–397.
- [16] A. Spira and R. Kimmel, "Geodesic curvature flow on parametric surfaces," in *Proc. Curve and Surface Design*, 2002, pp. 365–373.
- [17] A. Spira and R. Kimmel, "Segmentation of images painted on parametric manifolds," presented at the EUSIPCO, 2005.
- [18] S. Chen, B. Merriman, S. Osher, and P. Smereka, "A simple level set method for solving stefan problems," *J. Comput. Phys.*, vol. 135, no. 1, pp. 8–29, 1997.
- [19] G. Aubert and P. Kornprobst, *Mathematical Problems in Image Processing*. New York: Springer, 2002.
- [20] S. Kichenassamy, A. Kumar, P. Olver, A. Tannenbaum, and A. Yezzi, "Conformal curvature flows: From phase transitions to active vision," *Archive Rational Mech. Anal.*, vol. 134, pp. 275–301, 1996.
- [21] S. Osher, "Level set methods," in *Geometric Level Set Methods in Imaging, Vision and Graphics*, S. Osher and N. Paragios, Eds. New York: Springer-Verlag, 2003, pp. 3–20.
- [22] J. A. Sethian, *Level Set Methods and Fast Marching Methods: Evolving Interfaces in Computational Geometry, Fluid Mechanics, Computer Vision and Material Sciences*. Cambridge, U.K.: Cambridge Univ. Press, 1999.
- [23] X. Bresson, P. Vandergheynst, and J.-P. Thiran, "Multiscale active contours," in *Proc. 5th Int. Conf. Scale Space and PDE Methods in Computer Vision*, 2005, pp. 167–178.

- [24] N. Sochen, R. Kimmel, and R. Malladi, "A general framework for low level vision," *IEEE Trans. Image Process.*, vol. 7, no. 3, pp. 310–318, Mar. 1998.
- [25] N. Sochen, R. Kimmel, and R. Malladi, "A general framework for low level vision," Tech. Rep. LBNL-39243, Phys. Dept., Univ. California, Berkeley, 1996.
- [26] A. M. Polyakov, "Quantum geometry of bosonic strings," *Phys. Lett. B*, vol. 103, pp. 207–210, 1981.
- [27] C. L. Epstein and M. Gage, "The curve shortening flow," in *Wave Motion: Theory, Modeling, and Computation*, A. Chorin and A. Majda, Eds. New York: Springer-Verlag, 1987, vol. MR 89f:58128.
- [28] A. Spira and R. Kimmel, "Geometric curve flows on parametric manifolds," *J. Comput. Phys.*, 2006, accepted for publication.
- [29] "Animal eyes provide high-tech optical inspiration," *Nat. Geograph. News*, Dec. 2005.
- [30] R. Zbikowski, "Fly like a fly," *IEEE Spectrum*, vol. 42, no. 11, pp. 40–45, Nov. 2005.
- [31] J. Kovacevic and R. Murphy, "Molecular and cellular bioimaging," *IEEE Signal Processing Mag.*, vol. 23, no. 3, p. 19, Mar. 2006.

Iva Bogdanova was born in 1974 in Varshets, Bulgaria. She received the M.Sc. degree in telecommunications and the M.Sc. degree in applied mathematics from the Technical University of Sofia, Sofia, Bulgaria, in 1997 and 1999, respectively, and the Ph.D. degree from the Swiss Federal Institute of Technology, Lausanne (EPFL), Switzerland, in 2005.

In 2000, she joined the Signal Processing Institute (ITS), EPFL, as a Research Assistant. She is currently a Postdoctoral Researcher at the Institute of Microtechnology, Université de Neuchâtel, Neuchâtel, Switzerland. Her research interests are in harmonic analysis and processing data defined on curved manifolds.

Xavier Bresson was born in France, in 1976. He received the B.A. degree in theoretical physics from the University of Marseille I, Marseille, France, in 1998, the M.Sc. degree in electrical engineering from the Ecole Supérieure d'Electricité, Paris, France, the M.Sc. degree in automatism and signal processing from the University of Paris XI in 2000, and the Ph.D. degree in the field of computer vision from the Swiss Federal Institute of Technology, Lausanne (EPFL), Switzerland, in 2005.

He is currently a Postdoctorate in the Department of Mathematics, University of California, Los Angeles. His main research activities are focused on image segmentation and restoration using variational models, PDEs, differential geometry, and information theory, with a particular interest for medical image analysis.

Jean-Philippe Thiran (SM'96) was born in Namur, Belgium, in August 1970. He received the electrical engineering degree and the Ph.D. degree from the Université catholique de Louvain (UCL), Louvain-la-Neuve, Belgium, in 1993 and 1997, respectively.

He joined the Signal Processing Institute (ITS), Swiss Federal Institute of Technology (EPFL), Lausanne, Switzerland, in February 1998 as a Senior Lecturer. Since January 2004, he has been an Assistant Professor, responsible for the image analysis group. His current scientific interests include image segmentation, prior knowledge integration in image analysis, partial differential equations and variational methods in image analysis, multimodal signal processing, medical image analysis, including multimodal image registration, segmentation, computer-assisted surgery, diffusion MRI, etc. He is the author or coauthor of two book chapters, 58 journal papers, and some 92 peer-reviewed papers published in proceedings of international conferences. He holds four international patents.

Dr. Thiran was Co-Editor-in-Chief of the *Signal Processing* international journal (published by Elsevier Science) from 2001 to 2005. He is currently an Associate Editor of the *International Journal of Image and Video Processing*, published by Hindawi Publishing Corporation, and a member of the editorial board of the journal *Signal, Image and Video Processing*, published by Springer. He was a member of the organizing committee of the IEEE International Conference on Multimedia and Expo 2002 (ICME2002) and of the IEEE International Workshop on Neural Networks for Signal Processing 2002 (NNSP02) and a member of the scientific committees of many international conferences, including the IEEE International Conference on Image Processing (ICIP), the IEEE International Conference on Acoustics, Speech and Signal Processing (ICASSP), the IEEE Computer Society Conference on Computer Vision and Pattern Recognition (CVPR), the International Conference on Medical Image Computing and Computer Assisted Intervention (MICCAI), and the European Signal Processing Conference (EUSIPCO). He will be the General Chairman of the 2008 European Signal Processing Conference (EUSIPCO 2008).

Pierre Vanderghyest (M'01) received the M.S. degree in physics and the Ph.D. degree in mathematical physics from the Université catholique de Louvain, Louvain-la-Neuve, Belgium, in 1995 and 1998, respectively.

From 1998 to 2001, he was a Postdoctoral Researcher with the Signal Processing Laboratory, Swiss Federal Institute of Technology (EPFL), Lausanne, Switzerland. He is now an Assistant Professor at the EPFL, where his research focuses on harmonic analysis, information theory, sparse approximations, and mathematical image processing with applications to higher dimensional and complex data processing.

Dr. Vanderghyest was co-Editor-in-Chief of *Signal Processing* from 2002 to 2006.